Mining of Mineral Deposits
Volume 19 (2025), Issue 4, 53-62

MMD JOURNAL / MINING.IN.UA

https://doi.org/10.33271/mining19.04.053

Advanced CNN-based remote sensing for mineral mapping of porphyry systems in the Gilgit region

Muhammad Munzareen [1*]✉, Feroz Bibi [1]✉, Salman Ihsan [1]✉,
Kausar Sultan Shah [2]✉, Muhammad Zaka Emad [3]✉

[1] *Karakoram International University Gilgit, Gilgit Baltistan, Pakistan*
[2] *National University of Science & Technology, Balochistan Campus (NBC), Quetta, Pakistan*
[3] *King Fahd University of Petroleum and Minerals, Dhahran, Saudi Arabia*

**Corresponding author: e-mail muhammadmunzareen98@gmail.com*

Abstract

Purpose. This study aims to improve mineral identification in porphyry hydrothermal alteration zones, particularly in the challenging terrain of the Gilgit area, by combining remote sensing data with Convolutional Neural Networks (CNNs).

Methods. Landsat 8 Collection 2 Level 1 imagery from the United States Geological Survey (USGS) was processed using ENVI 5.3 software. Spectral Angle Mapping (SAM) classification was applied to identify alteration minerals. The dataset was then augmented, normalized, and split into training (75%), validation (15%), and testing (15%) sets. A CNN model incorporating convolutional, pooling, and fully connected layers was developed to perform binary classification of mineral compositions.

Findings. Advanced CNN-based remote sensing techniques have demonstrated significant potential in mapping porphyry systems. The CNN model achieved over 90% classification accuracy for minerals like feldspar and chalcocite, based on their spectral properties and dominant color features. This approach is beneficial in challenging terrains like Gilgit, where traditional methods can be difficult and expensive.

Originality. This study demonstrates the successful integration of remote sensing data with CNN-based algorithms for accurate mineral classification, providing a novel approach to overcoming the limitations of conventional field-based methods in challenging terrains.

Practical implications. The approach provides a practical and efficient solution for remote mineral exploration, particularly in regions with limited accessibility, supporting more accurate and faster geological assessments in the Gilgit area.

Keywords: *porphyry hydrothermal alteration zones, ENVI, convolutional neural network, remote sensing, normalization, data augmentation, classification*

1. Introduction

Remote sensing has provided tools for geological exploration for almost four decades. Nowadays, many satellite remote sensing datasets are accessible freely and can be extensively used for mineral exploration projects [1]. Geological maps help provide and investigate the locations of geological features associated with target mineralization, which is one of the most basic procedures in mineral exploration. These maps may contain features such as the lithological units, alteration types, structures, and indicator minerals [2]. Geological mapping technologies have evolved, and today, the combination of remote sensing data and modern data analytics, such as machine learning, is attracting significant interest [3]. This combination enables geologists to address the typical challenges associated with traditional methods, as illustrated in Figure 1 below.

In many environments where standard field surveys are complex and time-consuming, the application of remote sensing methods can distinguish mineralization based on associated lithological, structural, and hydrothermal change types [4]-[7]. These strategies are used in mineral exploration to identify structural features that may indicate controlled mineralization [8]. Remote sensing can effectively identify hydrothermal alteration zones due to changes in PCDs (porphyry copper deposits) caused by fluid expansion [9]. Remote sensing is frequently utilized for lithological and structural mapping, as well as mineral prospecting, which significantly reduces the expense of field research [10]. Mapping surface-altered rocks and their associated mineralization using satellite remote sensing photography is a valuable asset in any geological and mineral exploration operation [11].

Several studies have demonstrated the reliability of multispectral and hyperspectral remote sensing data processing in identifying hydrothermal alteration zones [12]. Scientists have been able to propose novel and efficient methods for data processing due to the extraordinary increase in the diversity of remote sensing data collected from various platforms and ground measurements [13].

Received: 28 April 2025. Accepted: 4 November 2025. Available online: 30 December 2025

Mining of Mineral Deposits. ISSN 2415-3443 (Online) | ISSN 2415-3435 (Print)

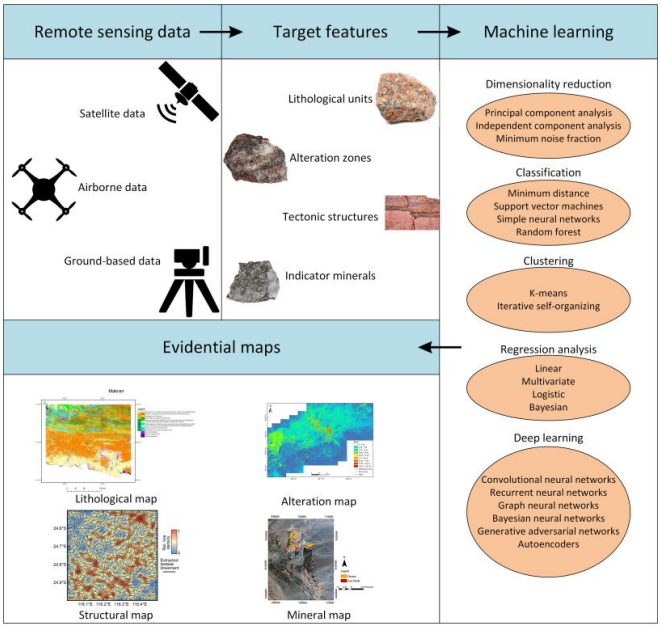

Figure 1. Integration of remote sensing & machine learning [14]

Over the past few decades, numerous image processing techniques have been developed to aid in the identification, differentiation, and enhancement of features such as lithological units, alteration zones, and structures using remote sensing data [14]. The Enhanced Thematic Mapper Plus (ETM+), Operational Land Imager (OLI), Advanced Spaceborne Thermal Emission and Reflection Radiometer (ASTER), and Hyperion are among the most recent multispectral and hyperspectral remote sensing instruments that have expanded the use of satellite imagery for mapping geological features [15]. The study of multispectral images is crucial for the exploration and identification of hydrothermally altered areas [16]. Remote sensing (ASTER) images with suitable spectral and spatial resolutions are utilized to identify hydrothermal alteration and structures effectively [17].

Economic mineralization is often formed through liquid processes, which significantly impact the mineralogy and chemistry of the host rock. This alteration can result in various mineral assemblages that differ depending on the location, intensity, and duration of the flow events. When exposed at the Earth's surface, this alteration can be traced occasionally in a zonal pattern, in the simplest instance, concentrically, around a core of highest-grade alteration and most economic significance [18]. Mapping alteration zones may benefit from the knowledge that remote sensing offers on the surface characteristics of exploration sites. Iron-rich and iron-poor lithologies are two examples of the different types of rocks that can be distinguished using broadband sensors, such as the Landsat Thematic Mapper (TM) and the SPOT (Satellite pour l'Observation de la Terre). Spectral absorptions in the visible to shortwave infrared specific to certain individual minerals can be detected using narrowband field devices like the Analytical Systems Devices (ASD) spectroradiometer.

Suppose these minerals are representative of the kind of alteration and sufficiently present at the surface to allow sun radiation to be reflected to the sensor. In that case, spectroradiometers hold the potential to be an invaluable supplementary data source for exploration geologists [18]. Potassic, phyllic, argillaceous, and propylitic zones are frequently seen in hydrothermally altered PCDs. These zones are shown to be coaxially oriented outward from a potassic core through phyllic, argillic, and propylitic zones [19]. Deep learning is a potent state-of-the-art method for analyzing images, particularly remote sensing (RS) images [20]. The integration of feature extraction and classifiers into learning frameworks has enabled deep learning to surpass the challenges associated with feature selection in previous methods. The goal of deep learning is to uncover multiple layers of representation, with the expectation that high-level characteristics will reflect the data's more abstract semantics. CNNs have been widely used in image categorization [21].

The study project aimed to identify porphyry hydrothermal alteration zones in the Gilgit region. This study was motivated by the need to investigate regions that are frequently inaccessible due to complex topography and severe weather conditions. The Gilgit region, renowned for its complex geological features, presents significant challenges to mineral exploration. Access to potential mineralization areas may be hindered by severe topography and variable weather patterns, making comprehensive geological investigations challenging. Our study aimed to address these challenges by mapping and analyzing hydrothermal alteration zones, which are characteristic of porphyry-type mineral deposits, and to develop a CNN model that classifies major minerals associated with porphyry hydrothermal alteration zones in the Gilgit Region.

2. Methods

2.1. Satellite data

Landsat satellites are well-known for their optical data, which is commonly used in geological mapping and other applications. For over 40 years, they have continuously monitored the Earth's surface to meet varied information and data requirements [22]. Data-acquiring platforms include satellites [23], [24]. Landsat 8 was launched on February 11, 2013, equipped with two sensors: OLI and a thermal infrared sensor, as shown in Figure 2.

Sensor	Spectral Band	Use Area	Wavelength	Resolution
OLI	Band 1	Coastal/Aerosol	0.433 – 0.453 µm	30 m
OLI	Band 2	Blue	0.450 – 0.515 µm	30 m
OLI	Band 3	Green	0.525 – 0.600 µm	30 m
OLI	Band 4	Red	0.630 – 0.680 µm	30 m
OLI	Band 5	Near Infrared	0.845 – 0.885 µm	30 m
OLI	Band 6	Short Wavelength Infrared (SWIR 1)	1.560 – 1.660 µm	30 m
OLI	Band 7	Short Wavelength Infrared (SWIR 2)	2.100 – 2.300 µm	30 m
OLI	Band 8	Panchromatic	0.500 – 0.680 µm	15 m
OLI	Band 9	Cirrus	1.360 – 1.390 µm	30 m
OLI	Band 10	Long Wavelength Infrared	10.30 – 11.30 µm	100 m
OLI	Band 11	Long Wavelength Infrared	11.50 – 12.50 µm	100 m

Figure 2. Properties of Landsat 8 OLI (eos.com)

It provides images with the exact resolution as ETM+ in 11 spectral bands, including VNIR and SWIR bands 1-7, as well as the panchromatic band 8. Band nine, which detects cirrus clouds, has a spatial resolution of 30 meters. The last two thermal bands (10 and 11) have a 100 m resolution. The OLI bands' spectral ranges aim to prevent atmospheric absorption inside the ETM+ bands [25]. ASTER is also a com-

ponent of the EOS Terra platform, which captures solar energy with 14 bands. The detection of ASTER reflected radiation within three bands extending from 0.52-0.86 μm in the VNIR, as well as the six bands for SWIR wavelengths extending between 1.6 and 2.43 μm, with resolution measured at 15 and 30 meters, respectively, for the VNIR and the SWIR range. In five TIR ASTER measurements, wavelengths have been recorded within the range of 8.125-11.65. Each scene in ASTER covers an area of 60 by 60 kilometers [26].

2.2. Convolutional neural network

Convolutional neural network is a type of neural network used to extract feature from any pattern. It consists of convolutional layers, pooling layer and fully connected layer. Specific parameters also include strike, padding, kernel size and number of kernels used in convolutional layers and pooling layers, as well as activation functions. These are some of most essential parts of CNN when making CNN architecture.

One of the most critical networks in the field of deep learning is a convolutional neural network (CNN). In recent years there has been considerable interest in CNNs from both industry and academia due to its significant accomplishments in various fields, such as computer vision and natural language processing [27]. CNN's architecture draws inspiration from the principles of visual perception. An artificial neuron is equivalent to a biological neuron; CNN kernels are several receptors that can react to distinct features. Activation functions simulate the function of neural electric signals that surpass a threshold, allowing them to pass on to the next neuron [27].

To be more precise, four parts are typically necessary to build a CNN model. Convolution is a vital stage in the feature extraction process. Convolutional outputs are known as feature maps. When setting a convolution kernel to a specific size, the information about the border is lost. Padding is used to increase the input with a zero value, hence indirectly changing its size. Additionally, the stride is used to control the convolution density. The density reduces with increasing stride length. After convolution, feature maps include a large number of features, increasing the danger of overfitting. To avoid duplication, pooling (also known as down-sampling) is proposed, which involves max pooling and average pooling [27].

Convolution, pooling, and fully connected layers are the three main types of layers (or building pieces) that make up a CNN in mathematics. The third layer, the fully connected layer, translates the extracted features into the final output, such as classification, while the first two layers, convolution and pooling, perform feature extraction. A crucial component of CNN is the convolution layer. CNN is composed of a series of mathematical operations, including convolution, a specific type of linear operation. Since a feature may exist in a digital image, CNNs are very effective for processing images because pixel values are kept in a two-dimensional (2D) grid, or an array of integers, and a small grid of parameters, called a kernel, an optimizable feature extractor, is applied to each image point anywhere in the picture. Complexity of retrieved characteristics can grow hierarchically and progressively, as one layer passes its output data to the next layer. Training is the process of fine-tuning parameters, such as kernels, using optimization algorithms like gradient descent and backpropagation, among others, to minimize the difference between outputs and ground truth labels [28]. The output feature maps of a convolutional neural network (CNN) are usually flattened into a one-dimensional (1D) vector, following the last convolution or pooling layer.

2.3. Study area

Gilgit-Baltistan, as shown in Figure 3, is the northernmost region of Pakistan. Islamabad, the capital of Pakistan, is primarily accessed through the Karakoram Highway, also known as the KKH. Geographically, this region is surrounded by Afghanistan to the northwest, China to the northeast, and Khyber Pakhtunkhwa to the southwest. This region is home to many towering mountains, with a few of them exceeding 8000 meters in height. Gilgit is also the administrative capital of Gilgit-Baltistan. The Gilgit region covers an area of about 16. housand km^2 [29].

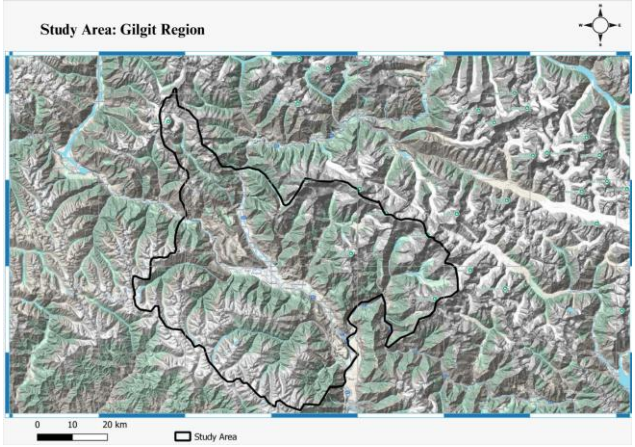

Figure 3. Study area map

The Gilgit area is primarily made up of river plain deposits. It is surrounded mainly by volcanic and Kohistan batholith rocks in the north, northeast, and northwest, while the Gilgit Complex meta-sedimentary rocks cover the southern, southeastern, and southwestern regions. The volcanic rocks are predominantly basaltic andesites, rhyolites, and pyroclastic flows. The Kohistan batholith is made up of several diorites, granodiorites, and granites [30].

2.4. Hydrothermal alteration zones

Hydrothermal alteration zones are areas where rocks have undergone chemical changes as a result of their interaction with hot, mineral-rich fluids. These modifications often occur in volcanic and tectonically active places, resulting in the creation of a variety of secondary minerals. These zones in Gilgit-Baltistan are notable for their association with valuable mineral reserves, primarily gold and base metals. Mineralization in hydrothermal alteration zones is visible in Figure 4.

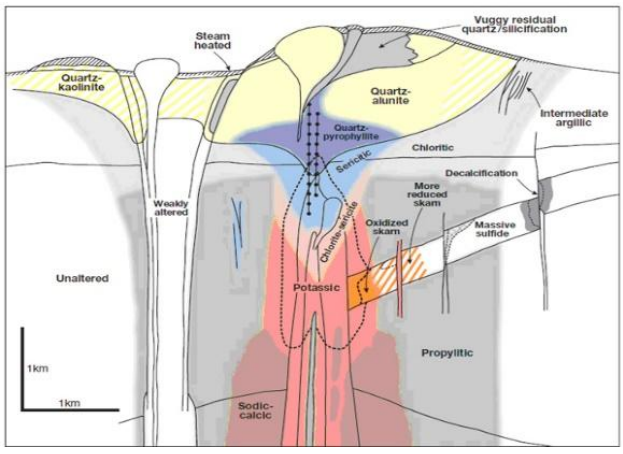

Figure 4. General mineralization of the hydrothermal alteration zone

In Gilgit-Baltistan, the principal minerals associated with hydrothermal alteration zones are chalcopyrite, a significant copper mineral found in sulfide deposits.

Pyrite, also known as "fool's gold" is frequently found in gold deposits and serves as an essential indicator of mineralization. Malachite and azurite are copper carbonate minerals that commonly form as secondary products in oxidized environments. Sericite, chlorite, and epidote are alteration products that indicate hydrothermal activity. They frequently result from the modification of feldspar and other silicate minerals.

The geological background of these changes is principally defined by volcanic rock formations, such as those found in the Chalt Volcanic Group and Shamaran volcanics, both of which are parts of the Kohistan Island Arc. The interaction of hydrothermal fluids with these rocks causes significant changes in their mineral composition, resulting in zones rich in economically valuable minerals, such as gold and copper.

2.5. Remote sensing methodology

The use of Landsat data to identify porphyry hydrothermal alteration zones is a complex procedure that requires several phases to achieve precise mineral detection. In this investigation, Landsat Collection 2 Level 1 imagery from Landsat 8, acquired by the USGS, was obtained on July 19, 2024. The data was processed using ENVI 5.3 software. Initially, the data was radiometrically calibrated to transform raw digital numbers into radiance values. This step is critical because it prepares the data for future atmospheric corrections. Following calibration, the FLAASH Atmospheric Correction method is employed to efficiently mitigate atmospheric interference, thereby enhancing the clarity of the spectral data. After minimizing the atmospheric impacts, the Math Band Expression was applied to normalize the data, thereby limiting the pixel values to a range of 0 to 1. This normalization is required for the comparative study and interpretation of spectral data.

To reliably identify the minerals associated with porphyry hydrothermal alteration zones, a spectral library was created using ENVI's built-in mineral spectral library, which comprises the spectral signatures of numerous minerals commonly observed in alteration zones. The developed spectral library matches the spectral signatures obtained from the image data and classifies minerals. The final step was the use of Spectral Angle Mapping (SAM) classification. This technique compares the spectral signatures of minerals in the spectral library to those found in Landsat imagery. Calculating the spectral angle allows us to properly detect and map the distribution of hydrothermal alteration minerals throughout the study area. Figure 5 explains the remote sensing methodology in a sequence.

Every mineral has a unique characteristic of its spectral range, which also differentiates it from other minerals. A spectrometer can measure the spectral range of minerals, and different minerals display distinct graphs with varying spectral ranges, as shown in Figure 6a-c. These graphs, given above, tell us about the spectral signatures of minerals formed in Hydrothermal Alteration Zones. Every mineral has a unique spectral signature.

2.6. Preprocessing of imagery satellite data through CNN

Using 13 distinct mineral labels, each associated with a specific color, a set of satellite images was analyzed in this study. To facilitate identification, the following minerals were color-coded: feldspar (magenta), chalcocite (lime green), pyrite (olive green), calcite (green), and epidote (blue).

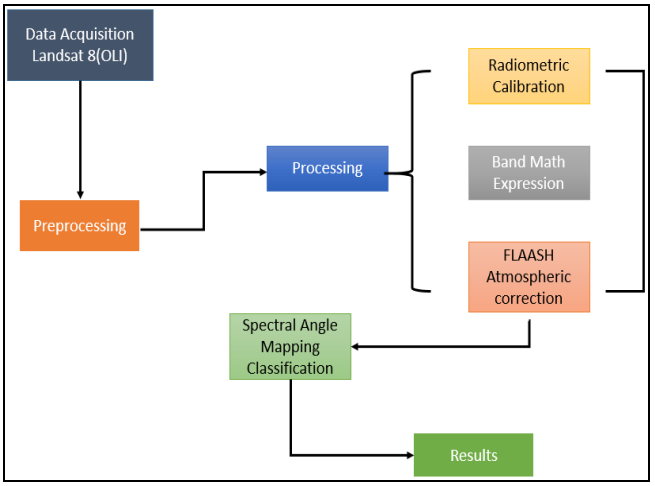

Figure 5. Flowchart of the remote sensing methodology

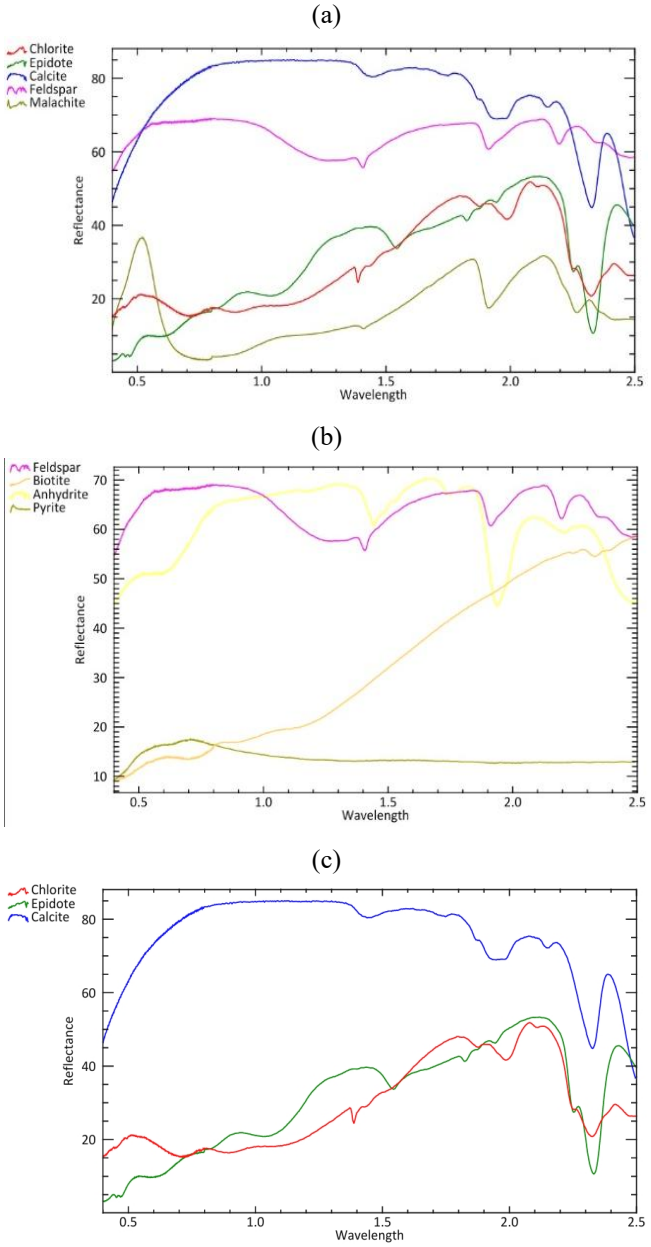

Figure 6. Spectral range of minerals in different hydrothermal alteration zones: (a) peripheral hydrothermal alteration zone; (b) potassic and phyllic hydrothermal alteration zone; (c) propylitic hydrothermal alteration zone

While the color coding functioned well in GIS and ENVI software, applying it with programming tools posed challenges. Malachite, serpentine, and chlorite were among the minerals difficult to identify accurately. This may be the result of program limitations, inconsistent color representation, or low-quality data. Our approach to addressing these challenges was targeted, and we chose two minerals: Chalcocite, which is relevant to copper, and Feldspar, which is relatively less common. Before extending the classification to all 13 minerals, this strategic choice enabled us to overcome the initial obstacles and enhance the model performance.

The dataset was preprocessed by segmenting the original satellite images, as shown in Figure 6, into 216 patches, each with dimensions of 302×302 pixels, as illustrated in Figure 7. Several augmentation techniques, including image rotation and flipping, were applied, resulting in approximately 4300 images. To improve data quality, this number was reduced to 3032 images. Background removal was a critical preprocessing step to eliminate high-intensity areas that hindered mineral feature extraction, particularly for Feldspar and Chalcocite.

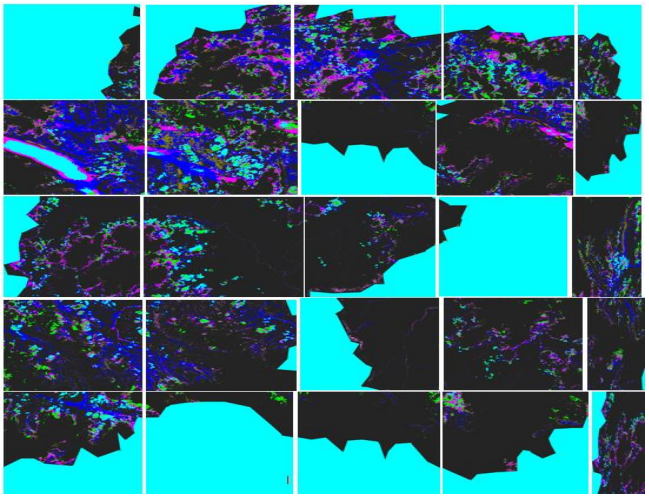

Figure 7. Pacifying image

The dataset was structured into three sets: training, validation, and testing, with a split of 70, 15 and 15%, respectively. Each set contained an equal number of images for Feldspar and Chalcocite. This organized dataset arrangement ensured the practical training of machine learning models, where the validation set was used for hyperparameter tuning, and the test set assessed the model generalization capability. By employing a systematic approach to data preparation and augmentation, we aimed to enhance the classification accuracy and robustness of the model for the selected minerals. Figures 8 and 9 illustrate the overall preprocessing stages through programming.

The flowchart in Figure 9 shows the preprocessing steps involved in CNN training. Imagery data from GIS and Envi is prepared through programming and then further processed through steps such as patching, which divides large images into smaller parts; data augmentation, which increases the dataset by transformation; extracting relevant features; normalization; and data splitting and organization. The reason behind the preprocessing steps is to clean and prepare the imagery data for the CNN model.

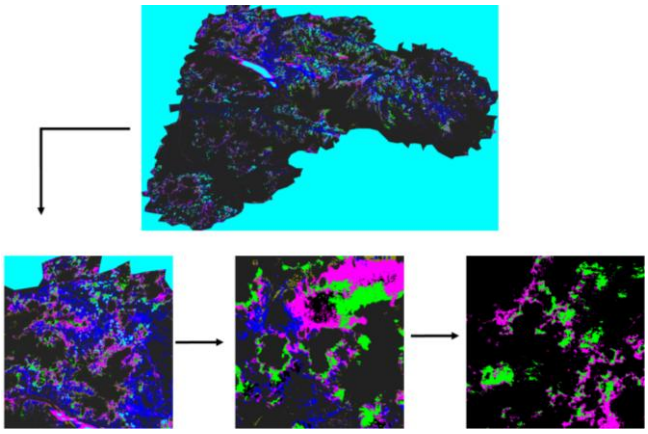

Figure 8. Preprocessing images

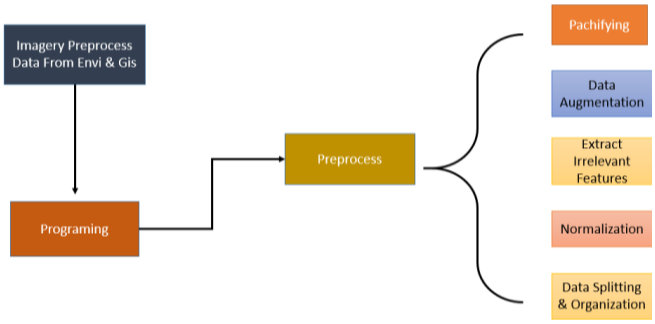

Figure 9. Preprocessing through programming

2.7. Convolutional neural network model

To categorize mineral images, this study developed a Convolutional Neural Network (CNN) with a focus on feldspar and chalcocite. A 150×150 feature map is produced by the CNN's Conv2D layer, which uses 32 filters of size 3×3 to extract fundamental characteristics, such as edges. To save computational costs and preserve essential characteristics, a MaxPooling2D layer is used to shrink the spatial dimensions to 75×75. Next, the network adds additional Conv2D layers, gradually reducing the feature map to 8×8 and increasing the filter count to 128. As the network becomes deeper, these layers can collect progressively more complex characteristics. Based on the likelihood of the affirmative class, the architecture's last dense layer produces a binary classification, as shown in Figure 10.

The train generator's batches were used to train the model using a fit function, and the validation data was used to assess the model performance. The model performed well in categorizing unknown data, with a test accuracy of 95.09% after 10 epochs of training. The trained model was also used to categorize fresh photos. After being scaled, normalized, and run through the model, the images were effectively classified as either Feldspar or Chalcocite, depending on a threshold value. The visualization model is shown in Figure 11.

Figure 11 shows the architecture and parameters used for image classification in the CNN model. The model includes several convolutional and pooling layers that smoothly extract the spatial features in the imagery data. In the second layer, the output is flattened and passes through a dense layer, which learns the complex patterns and relationships within the imagery data. To prevent model overfitting, a dropout layer is added, which also aids in model generalization. In short, the model contains 4.37 million trainable parameters, reflecting its depth of capability to correctly analyze and classify imagery data as required in this study.

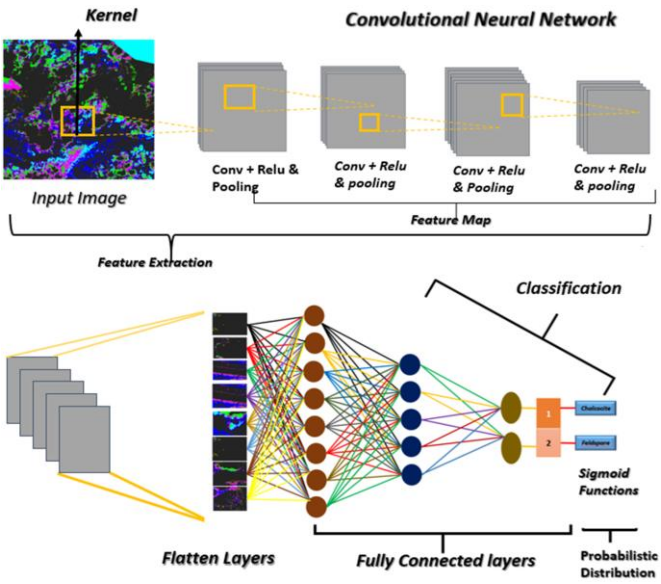

Figure 10. Architecture of CNN

Model: "sequential_8"

Layer (type)	Output Shape	Param #
conv2d_26 (Conv2D)	(None, 150, 150, 32)	896
max_pooling2d_26 (MaxPooling2D)	(None, 75, 75, 32)	0
conv2d_27 (Conv2D)	(None, 73, 73, 32)	9,248
max_pooling2d_27 (MaxPooling2D)	(None, 37, 37, 32)	0
conv2d_28 (Conv2D)	(None, 37, 37, 64)	18,496
max_pooling2d_28 (MaxPooling2D)	(None, 18, 18, 64)	0
conv2d_29 (Conv2D)	(None, 16, 16, 128)	73,856
max_pooling2d_29 (MaxPooling2D)	(None, 8, 8, 128)	0
flatten_8 (Flatten)	(None, 8192)	0
dense_16 (Dense)	(None, 512)	4,194,816
dropout_8 (Dropout)	(None, 512)	0
dense_17 (Dense)	(None, 1)	513

Total params: 4,297,825 (16.39 MB)
Trainable params: 4,297,825 (16.39 MB)
Non-trainable params: 0 (0.00 B)

Figure 11. CNN model

3. Results and discussion

The production of minerals within hydrothermal alteration zones is widely documented in geological literature. When mineral-rich fluids contact host rocks, they undergo hydrothermal alteration, resulting in significant changes in mineralogical composition. A variety of elements influence this process, including the temperature, pressure, and chemical composition of the hydrothermal fluids, as well as the type of host rocks. In this investigation, Spectral Angle Mapping (SAM) classification was performed to identify minerals associated with porphyry and other hydrothermal alteration zones. QGIS was used to produce these Hymaps. This classification technique detects the presence of minerals in remote sensing data by using their spectral signature. Minerals of porphyry hydrothermal alteration zones were identified using the SAM classification, including epidote, calcite, and chlorite, as shown in Figure 12a.

Minerals formed in porphyry hydrothermal alteration zones are classified based on spectral signatures. In addition to discovering porphyry hydrothermal alteration zones, our investigation indicated the presence of additional hydrothermal alteration zones in the Gilgit and surrounding areas, as shown in Figure 12b-c.

In both the training and validation sets, the model initially showed promising results with modest accuracy and losses throughout the learning process. Accuracy increased gradually as training progressed, but overfitting began to emerge, with the model performing significantly better on the training data than on the validation data. Despite this, the model continued to improve, eventually achieving very high accuracy and minimal loss on both sets, particularly in the later epochs. Although the model achieved 100% accuracy on the training set, its performance on the validation set marginally decreased, indicating some difficulty in generalizing new data.

The output illustrates the comparison between training and validation accuracy, as well as the changes in training and validation loss during training, as shown in Table 1.

Table 1. Model accuracy & loss

Epoch	Training accuracy, %	Training loss	Validation accuracy	Validation loss, %
1	49.34	0.7728	76.82	46.81
2	71.88	0.4562	73.33	37.23
3	86.00	0.3805	93.75	17.12
4	96.88	0.1742	86.67	23.22
5	90.48	0.2524	95.57	11.34
6	93.75	0.2267	93.33	17.86
7	95.47	0.1365	89.32	33.19
8	100.00	0.0356	73.33	40.59
9	95.09	0.1473	94.27	16.04
10	96.88	0.046	93.33	5.41

The validation accuracy and loss fluctuate initially, indicating that the model is adapting to the data and that there may be occasional instances of overfitting or underfitting. The model attempts to generalize from training data to validation data, so this volatility is typical of early epochs. However, the model performance was enhanced by changing a few crucial parameters, including the learning rate, the dropout rate, and the number of convolutional layers. To avoid overfitting or underfitting and maintain a balance in learning, these parameters are essential. By arbitrarily turning off neurons during training, dropout enhances generalization by preventing the model from remembering the training set. Adjusting the learning rate enables the model to learn at a speed that prevents overshooting ideal values or learning too slowly, and adding more convolutional layers improves the model capacity to extract more complex features from the input data. As a result, the validation accuracy initially increased and occasionally surpassed the training accuracy. This phenomenon, in which the model performs momentarily better on previously unseen data, may be attributed to the regularization effect of dropout and learning rate adjustments. However, as the epochs progress, the validation accuracy fluctuates and initially tends to decline before gradually catching up to the training accuracy. Both accuracies eventually stabilize and improve.

The validation loss exhibits a similar pattern, initially rising, which suggests that the model has difficulty in generalizing. However, as the model gains more experience, the loss decreases, indicating improved results of both the training and validation sets. Both training and validation loss decline gradually over time, indicating that the model is learning efficiently and avoiding overfitting.

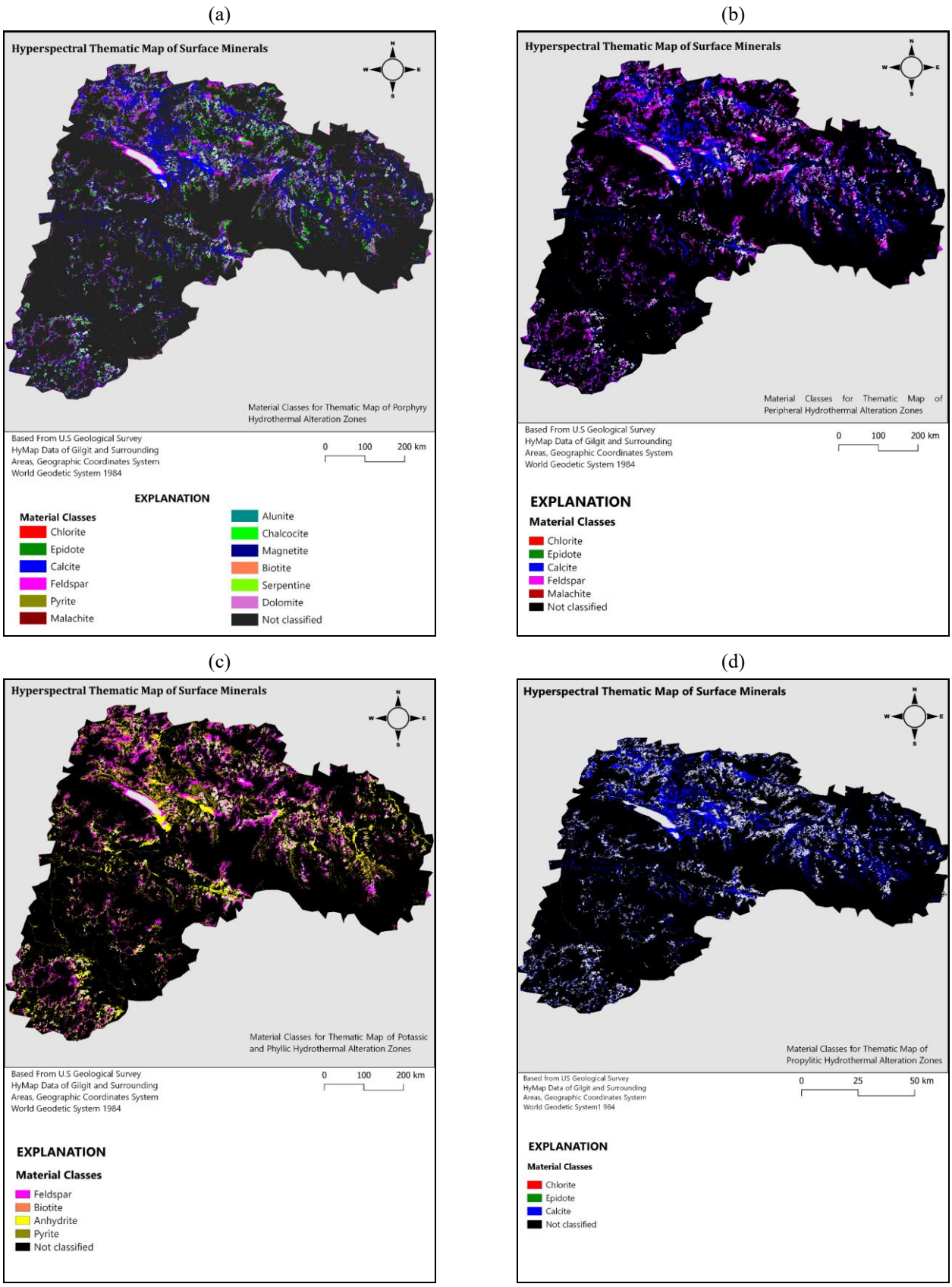

Figure 12. Hymaps of porphyry hydrothermal alteration zones: (a) porphyry hydrothermal alteration zones; (b) peripheral hydrothermal alteration zones; (c) potassic and phyllic alteration zones; (d) propylitic hydrothermal alteration zones

In summary, the adjustments made to the model architecture and learning parameters enabled it to overcome initial fluctuations and fit well to both the training and validation data, as shown in Figure 13. The steady alignment of validation accuracy with training accuracy, and the decrease in loss, suggest that the model effectively learned from the data and established a balance between learning from the training data and generalizing to unseen validation data.

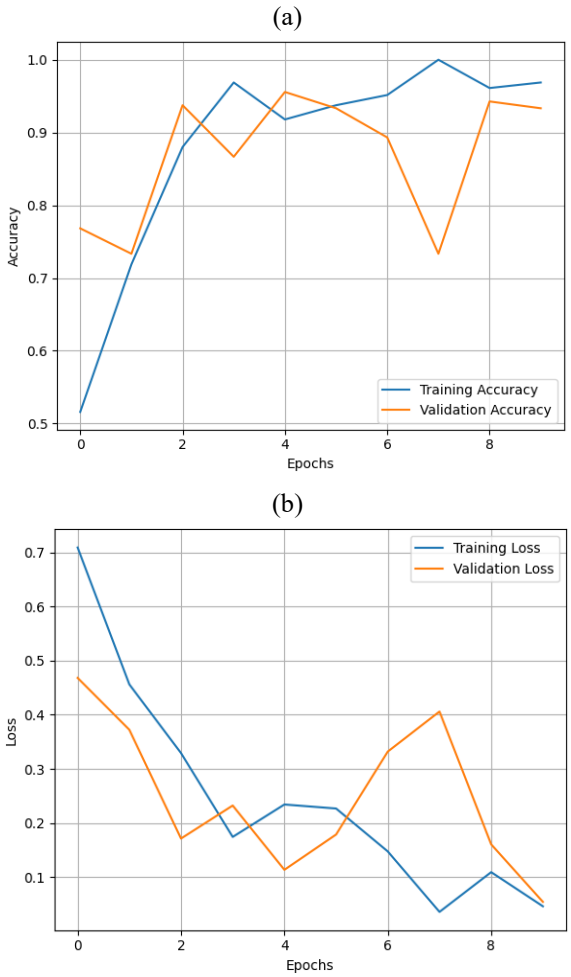

Figure 13. Comparison of model performance metrics: (a) training and validation accuracy; (b) training and validation loss

With a low test loss of 0.0936 and a high test accuracy of 95.09%, the model demonstrated exemplary performance and minimal prediction error. Table 2 highlights the model accuracy percentage and loss.

Table 2. Model accuracy & loss

Dataset	Accuracy (%)	Loss (%)
Training	96	0.967
Validation	93.33	0.152
Test	92.87	0.2595

It efficiently categorizes minerals by examining the pixel proportions of a scaled and normalized TIFF image, using the unique RGB values of Feldspar (magenta) and Chalcocite (green) as shown in Figure 14. The method computes percentages, shows the results, and compares pixels to the preset RGB values. Geographical software, such as ENVI or GIS, is then used to map the distribution of minerals and extract geographic information, as shown in Figure 15. To facilitate mining, resource management, and environmental protection applications, this method helps pinpoint the exact locations of minerals.

The classification of minerals based on color pixels is shown in Figure 14. The green areas in the figure indicate chalcopyrite, and the pink areas show feldspar. The reason for using color-based classification in this study is to identify and separate different minerals in the imagery data, which in turn helps in understanding their distribution within the study area.

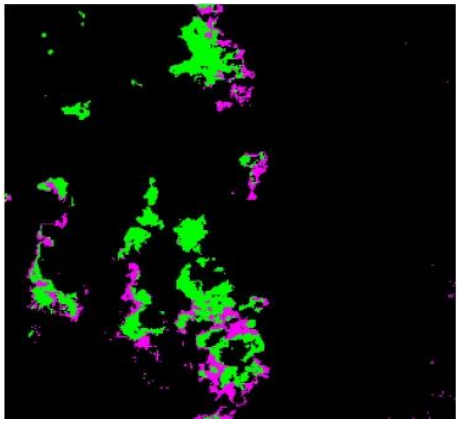

Figure 14. Classification based on color pixels (chalcocite – 5.27%; feldspar – 2.72%)

Figure 15. Extracted coordinates through ENVI

The coordinates of the imagery data are extracted using ENVI software, as shown in Figure 15. These coordinates mark the exact locations in the study area, which will help with real-world ground positions in the future. This was important, as it gives confidence in the accuracy and precision required for model development.

4. Conclusions

Spectral Angle Mapping classification was used to identify the minerals formed in porphyry hydrothermal alteration zones. A spectral library was prepared to identify the minerals formed in porphyry hydrothermal alteration zones. The Spectral Angle Mapping classification algorithm was run, which matches the spectral signatures found in the satellite imagery with those provided in the spectral library. Identified minerals include Chlorite, Chalcocite, Pyrite, Epidote, Malachite, Calcite, Alunite, Magnetite, Biotite, Serpentine, Dolomite and Feldspar. On the other hand, a Convolutional Neural Network model was developed to classify minerals based on the pixel values of their colors. Using satellite images as a guide, we successfully created and deployed a Convolutional Neural Network (CNN) model to categorize minerals, with a focus on Chalcocite and Feldspar due to their distinctive color patterns. Chalcocite (“#00FE00”) and Feldspar (“#FE00FE”) are the two distinct color codes assigned to each mineral, which allowed the model to distinguish between them with great accuracy. These color codes were used in the categorization procedure.

We increased the size of our dataset to 3000 images by using image augmentation techniques, which guarantees a

stable and varied dataset for testing, validation, and training. The training (70%), validation (15%), and testing (15%) sets of data enabled efficient assessment of the model performance. To determine whether a picture represented Feldspar or Chalcocite, the CNN architecture used consisted of multiple Conv2D and MaxPooling2D layers, followed by a fully connected Dense layer with a binary classification output. The developed model achieves training accuracy and loss of 96% and 0.967%, respectively, with a validation accuracy of 93.33% and a validation loss of 0.152%. Moreover, the test accuracy is 92.87%, and the test loss is 0.2595%.

Author contributions

Conceptualization: MM, FB, SI, KSS; Data curation: MM, FB; Formal analysis: MM, FB, SI, KSS; Investigation: MM, SI, KSS; Methodology: MM, SI, MZE; Project administration: KSS, MZE; Resources: KSS, MZE; Software: SI, MZE; Supervision: KSS, MZE; Validation: MM, FB, SI; Visualization: MM, FB; Writing – original draft: MM, FB, SI, KSS; Writing – review & editing: MZE. All authors have read and agreed to the published version of the manuscript.

Funding

This research received no external funding.

Conflicts of interest

The authors declare no conflict of interest.

Data availability statement

The original contributions presented in the study are included in the article, further inquiries can be directed to the corresponding author.

References

[1] Sekandari, M., Masoumi, I., Beiranvand Pour, A., Muslim, A.M., Rahmani, O., Hashim, M., Zoheir, B., Pradhan, B., Misra, A., & Aminpour, S.M. (2020). Application of Landsat-8, Sentinel-2, ASTER and Worldview-3 spectral imagery for exploration of carbonate-hosted Pb-Zn deposits in the Central Iranian Terrane (CIT). *Remote Sensing*, *12*(8), 1239. https://doi.org/10.3390/rs12081239

[2] Brimhall, G.H., Dilles, J.H., & Proffett, J.M. (2005). The role of geologic mapping in mineral exploration. *Wealth Creation in the Minerals Industry*, 221-241. https://doi.org/10.5382/SP.12.11

[3] Cracknell, M.J., & Reading, A.M. (2014). Geological mapping using remote sensing data: A comparison of five machine learning algorithms, their response to variations in the spatial distribution of training data and the use of explicit spatial information. *Computers & Geosciences*, *63*, 22-33. https://doi.org/10.1016/j.cageo.2013.10.008

[4] El Janati, M. (2019). Application of remotely sensed ASTER data in detecting alteration hosting Cu, Ag and Au bearing mineralized zones in Taghdout area, Central Anti-Atlas of Morocco. *Journal of African Earth Sciences*, *151*, 95-106. https://doi.org/10.1016/j.jafrearsci.2018.12.002

[5] Eslami, A., Ghaderi, M., Rajendran, S., Pour, A.B., & Hashim, M. (2015). Integration of ASTER and Landsat TM remote sensing data for chromite prospecting and lithological mapping in Neyriz ophiolite zone, South Iran. *Resource Geology*, *65*(4), 375-388. https://doi.org/10.1111/rge.12076

[6] Salaj, S.S., Srivastava, S.K., Dugal, R., Upadhyay, R., Suresh Babu, D.S., & Kaliraj, S. (2018). Application of ASTER remote sensing for lithological mapping in the Udaipur District of Rajasthan, India. *Applications and Challenges of Geospatial Technology*, 99-119. https://doi.org/10.1007/978-3-319-99882-4_7

[7] Xu, Y., Chen, J., & Meng, P. (2019). Detection of alteration zones using hyperspectral remote sensing data from Dapingliang skarn copper deposit and its surrounding area, Shanshan County, Xinjiang Uygur autonomous region, China. *Journal of Visual Communication and Image Representation*, *58*, 67-78. https://doi.org/10.1016/j.jvcir.2018.11.032

[8] Ciampalini, A., Garfagnoli, F., Antonielli, B., Moretti, S., & Righini, G. (2012). Remote sensing techniques using Landsat ETM+ applied to the detection of iron ore deposits in Western Africa. A*rabian Journal of Geosciences*, *6*(11), 4529-4546. https://doi.org/10.1007/s12517-012-0725-0

[9] Hosseinjani, M., & Tangestani, M.H. (2011). Mapping alteration minerals using sub-pixel unmixing of ASTER data in the Sarduiyeh area, SE Kerman, Iran. *International Journal of Digital Earth*, *4*(6), 487-504. https://doi.org/10.1080/17538947.2010.550937

[10] Amer, R., Kusky, T., & El Mezayen, A. (2012). Remote sensing detection of gold related alteration zones in Um Rus area, Central Eastern Desert of Egypt. *Advances in Space Research*, *49*(1), 121-134. https://doi.org/10.1016/j.asr.2011.09.024

[11] Traore, M., Takodjou Wambo, J.D., Ndepete, C.P., Tekin, S., Pour, A.B., & Muslim, A.M. (2020). Lithological and alteration mineral mapping for alluvial gold exploration in the south east of Birao area, Central African Republic using Landsat-8 Operational Land Imager (OLI) data. *Journal of African Earth Sciences*, *170*, 103933. https://doi.org/10.1016/j.jafrearsci.2020.103933

[12] Mars, J.C., & Rowan, L.C. (2010). Spectral assessment of new ASTER SWIR surface reflectance data products for spectroscopic mapping of rocks and minerals. *Remote Sensing of Environment*, *114*(9), 2011-2025. https://doi.org/10.1016/j.rse.2010.04.008

[13] Ali, I., Greifeneder, F., Stamenkovic, J., Neumann, M., & Notarnicola, C. (2015). Review of machine learning approaches for biomass and soil moisture retrievals from remote sensing data. *Remote Sensing*, *7*(12), 16398-16421. https://doi.org/10.3390/rs71215841

[14] Shirmard, H., Farahbakhsh, E., Müller, R.D., & Chandra, R. (2022). A review of machine learning in processing remote sensing data for mineral exploration. *Remote Sensing of Environment*, *268*, 112750. https://doi.org/10.1016/j.rse.2021.112750

[15] Rezaei, A., Hassani, H., Moarefvand, P., & Golmohammadi, A. (2019). Lithological mapping in Sangan region in Northeast Iran using ASTER satellite data and image processing methods. *Geology, Ecology, and Landscapes*, *4*(1), 59-70. https://doi.org/10.1080/24749508.2019.1585657

[16] Zamyad, M., Afzal, P., Pourkermani, M., Nouri, R., & Jafari, M.R. (2019). Determination of hydrothermal alteration zones using remote sensing methods in Tirka Area, Toroud, NE Iran. *Journal of the Indian Society of Remote Sensing*, *47*(11), 1817-1830. https://doi.org/10.1007/s12524-019-01032-3

[17] Asl, R.A., Afzal, P., Adib, A., & Yasrebi, A.B. (2015). Application of multifractal modeling for the identification of alteration zones and major faults based on ETM+ multispectral data. *Arabian Journal of Geosciences*, *8*(5), 2997-3006. https://doi.org/10.1007/s12517-014-1366-2

[18] Ferrier, G., White, K., Griffiths, G., Bryant, R., & Stefouli, M. (2002). The mapping of hydrothermal alteration zones on the island of Lesvos, Greece using an integrated remote sensing dataset. *International Journal of Remote Sensing*, *23*(2), 341-356. https://doi.org/10.1080/01431160010003857

[19] Fu, H., Cheng, Q., Jing, L., & Ge, Y. (2021). Deep learning-based hydrothermal alteration mapping using GaoFen-5 hyperspectral data in the Duolong Ore District, Western Tibet, China. *Journal of Applied Remote Sensing*, *15*(4), 044512. https://doi.org/10.1117/1.jrs.15.044512

[20] Kussul, N., Lavreniuk, M., Skakun, S., & Shelestov, A. (2017). Deep learning classification of land cover and crop types using remote sensing data. *IEEE Geoscience and Remote Sensing Letters*, *14*(5), 778-782. https://doi.org/10.1109/lgrs.2017.2681128

[21] Yan, Z., Piramuthu, R., Jagadeesh, V., Di, W., & Decoste, D. (2019). *Hierarchical deep convolutional neural network for image classification*. Google Patents.

[22] Wulder, M.A., White, J.C., Goward, S.N., Masek, J.G., Irons, J.R., Herold, M., Cohen, W.B., Loveland, T.R., & Woodcock, C.E. (2008). Landsat continuity: Issues and opportunities for land cover monitoring. *Remote Sensing of Environment*, *112*(3), 955-969. https://doi.org/10.1016/j.rse.2007.07.004

[23] Prost, G.L. (2013). *Remote sensing for geoscientists*. London, United Kingdom: CRC Press, 702 p. https://doi.org/10.1201/b15638

[24] Toth, C., & Jóźków, G. (2016). Remote sensing platforms and sensors: A survey. *ISPRS Journal of Photogrammetry and Remote Sensing*, *115*, 22-36. https://doi.org/10.1016/j.isprsjprs.2015.10.004

[25] Zhang, T., Yi, G., Li, H., Wang, Z., Tang, J., Zhong, K., Li, Y., Wang, Q., & Bie, X. (2016). Integrating data of ASTER and Landsat-8 OLI (AO) for hydrothermal alteration mineral mapping in Duolong Porphyry Cu-Au Deposit, Tibetan Plateau, China. *Remote Sensing*, *8*(11), 890. https://doi.org/10.3390/rs8110890

[26] Rowan, L.C., & Mars, J.C. (2003). Lithologic mapping in the Mountain Pass, California area using advanced spaceborne thermal emission and reflection radiometer (ASTER) data. *Remote Sensing of Environment*, *84*(3), 350-366. https://doi.org/10.1016/s0034-4257(02)00127-x

[27] Li, Z., Liu, F., Yang, W., Peng, S., & Zhou, J. (2022). A survey of convolutional neural networks: analysis, applications, and prospects. *IEEE Transactions on Neural Networks and Learning Systems*, *33*(12), 6999-7019. https://doi.org/10.1109/tnnls.2021.3084827

[28] Yamashita, R., Nishio, M., Do, R.K.G., & Togashi, K. (2018). Convolutional neural networks: an overview and application in radiology. *Insights into Imaging*, *9*(4), 611-629. https://doi.org/10.1007/s13244-018-0639-9

[29] Ahmad, L., Shah, M.T., & Khan, S.D. (2016). Reflectance spectroscopy and remote sensing data for finding sulfide-bearing alteration zones and mapping geology in Gilgit-Baltistan, Pakistan. *Earth Science Informatics*, *9*(1), 113-121. https://doi.org/10.1007/s12145-015-0239-x

[30] Khan, S., Rehman, S., Zeb Khan, A., Amjad Khan, M., & Tahir Shah, M. (2010). Soil and vegetables enrichment with heavy metals from geological sources in Gilgit, northern Pakistan. *Ecotoxicology and Environmental Safety*, *73*(7), 1820-1827. https://doi.org/10.1016/j.ecoenv.2010.08.016

Передові технології дистанційного зондування на основі CNN для створення карт мінеральних ресурсів порфірових систем у регіоні Гілгіт

М. Мунзарін, Ф. Бібі, С. Іхсан, К.С. Шах, М.З. Емад

Мета. Вдосконалення ідентифікації мінералів у зонах порфірової гідротермальної альтерації, особливо у складному гірському рельєфі району Гілгіт, шляхом інтеграції даних дистанційного зондування зі згортковими нейронними мережами (CNN).

Методика. Використано супутникові знімки Landsat 8 Collection 2 Level 1, отримані з бази United States Geological Survey (USGS). Їх оброблено у програмному забезпеченні ENVI 5.3 із застосуванням методу класифікації Spectral Angle Mapping (SAM) для виявлення зон мінеральних змін. Набір даних було розширено шляхом аугментації, нормалізовано та розподілено на навчальну (75%), валідаційну (15%) і тестову (15%) вибірки. Створено модель CNN, яка включає згорткові, пулінгові та повнозв'язні шари для бінарної класифікації мінеральних складів.

Результати. Доведено, що передові CNN-методи дистанційного зондування демонструють високу ефективність у картуванні мінералів порфірових систем. Встановлено, що розроблена модель нейронної мережі досягла точності навчання понад 96% та валідації 93.3% для таких мінералів як польовий шпат і халькоцит, завдяки їх спектральним характеристикам і домінантним кольоровим ознакам. Визначено, що запропонований підхід виявився особливо корисним у важкодоступних гірських регіонах, зокрема в районі Гілгіт, де традиційні методи є складними та затратними.

Наукова новизна. Уперше продемонстровано успішну інтеграцію даних дистанційного зондування з алгоритмами на основі CNN для точної класифікації мінералів у зонах порфірової альтерації, що дозволяє подолати обмеження польових методів у складних природних умовах.

Практична значимість. Розроблений підхід забезпечує ефективний інструмент для дистанційної розвідки мінеральних ресурсів у важкодоступних районах, сприяючи підвищенню точності та швидкості геологічних оцінок у межах району Гілгіт.

Ключові слова: *зони порфірової гідротермальної альтерації, ENVI, згорткова нейронна мережа, дистанційне зондування, нормалізація, аугментація даних, класифікація*

Publisher's note

All claims expressed in this manuscript are solely those of the authors and do not necessarily represent those of their affiliated organizations, or those of the publisher, the editors and the reviewers.